



Cite this: *RSC Adv.*, 2021, 11, 6464

Atmospheric plasma reaction synthesised $\text{Pt}_x\text{Fe}_{1-x}$ /graphene and TiO_2 nanoparticles/graphene for efficient dye-sensitized solar cells†

Xiaoyu Cao, Qingyu Shen, Yefei Zhuang, Guoce Zhuang* and Xiaobo Chen *

We report a facile atmospheric plasma reaction synthesis of $\text{Pt}_x\text{Fe}_{1-x}$ alloys with the different Pt/Fe stoichiometric ratio in $\text{Pt}_x\text{Fe}_{1-x}$ alloys on graphene (G) as efficient counter electrode (CE) materials and atmospheric plasma reaction synthesised TiO_2 nanoparticles/G as photoanode in dye-sensitized solar cells (DSSCs). Well-distributed $\text{Pt}_x\text{Fe}_{1-x}$ nanoparticles or TiO_2 nanoparticles on the G surface were obtained. Remarkably, DSSCs prepared by the $\text{Pt}_{0.7}\text{Fe}_{0.3}$ /G CE have much higher catalytic activity and stable durability than Pt_1Fe_0 /G CE. The as-synthesized $\text{Pt}_{0.7}\text{Fe}_{0.3}$ /G CE exhibits the largest value of $|J_{\text{red}}| = 1.479 \text{ mA}$ and the lowest value of $R_{\text{ct}} = 2.86 \Omega$. With the $\text{Pt}_{0.7}\text{Fe}_{0.3}$ /G as CE and TiO_2 /G as the photoanode, the DSSC can deliver an overall power conversion efficiency (PCE) of 10.13%, which is significantly higher than the 9.72% of the expensive Pt_1Fe_0 /G counterpart. The obtained results indicate that the $\text{Pt}_x\text{Fe}_{1-x}$ /G nanohybrids fabricated using atmospheric plasma reaction exhibited potential as a reference for next generation CE materials in highly efficient DSSCs. We believe that this work provides an effective strategy for optimizing Pt utilization for the low-cost and efficient application of DSSCs.

Received 28th November 2020

Accepted 30th January 2021

DOI: 10.1039/d0ra10067f

rsc.li/rsc-advances

1. Introduction

The dye-sensitized solar cells (DSSCs) are considered to be a promising alternative to commercial silicon solar cells.^{1–3} The reduction of I_3^- to I^- ions is critical in efficient DSSC devices. Generally, the precious platinum (Pt) has been employed as the best counter electrode (CE) material due to its high electrical conductivity and superior electrocatalytic activity to the I_3^-/I^- redox system.⁴ In typical standard DSSCs, a high Pt loading is required in order to improve the CE properties, which results in increases in the cost of DSSCs. Therefore, one of the best approaches to develop effectively and low-cost CE materials are by reducing precious Pt without compromising the electrochemical performance. Furthermore, improvement of the long-term stability of Pt CE under corrosion in the electrolyte is still a significant obstacle. For this reason, the reduction of particle size of Pt catalyst to nanoscale and dispersing them on proper support matrix are adopted. Carbon materials in various forms like graphene (G), graphite and carbon black are still the mostly used materials for DSSCs because of their high conductivity, availability and low cost.^{5–7} Moreover, increasing the intrinsic catalytic activity of Pt by alloying it with transition metals (Ni, Co, Fe, Mo, and Cu) is also a promising method.^{8–10} Hence, under the background of developing efficient low-cost hybrid

CE materials, several PtM alloys/G ($\text{M} = \text{Ni}, \text{Co}, \text{Pd}, \text{Fe}, \text{Mo}, \text{Cu}, \text{Cr}, \text{Sn}, \text{and Ru}$) as materials for CEs have been developed, and these study results have demonstrated them to be good CE alternatives to traditional Pt electrode.^{11–13} In searching for efficient low-Pt nanohybrid CEs, in the current work, we present here the synthesis of $\text{Pt}_x\text{Fe}_{1-x}$ alloy/G nanohybrid CEs and the optimization of $\text{Pt}_x\text{Fe}_{1-x}$ /G for highly photovoltaic efficiency of DSSCs. It is expected that the optimized $\text{Pt}_x\text{Fe}_{1-x}$ /G nanocomposite will combine both good conductivity and high catalytic activity in the reduction reaction of I^-/I_3^- .

For coating the PtM alloys ($\text{M} = \text{Ni}, \text{Co}, \text{Pd}, \text{Fe}, \text{Mo}, \text{Cu}, \text{Cr}, \text{Sn}, \text{and Ru}$) on a conductive substrate, several conventional methods (such as sputtering, electrochemical deposition and hydro-thermal chemical reduction) have been developed.^{11–13} However, these methods usually need high temperatures and vacuum condition. To overcome these disadvantages, plasma technology has been developed to synthesize bimetallic nanoparticles.^{13–16} Atmospheric plasma reaction technology is operated at under room temperature and pressure conditions. In the atmospheric plasma reaction process, some species in the aqueous solution near the plasma can be transformed into highly reactive species, which can rapidly react with other surrounding highly reactive species to form products.^{13,15} This plasma technology is particularly compatible with the fabrication process of DSSCs, which also requires no vacuum system. This is one main advantage of DSSCs over other photovoltaic cells.^{17–21} It is important to note that this approach only requires a short aging time for reduction and nearly room temperature. One of the main motivations in this work is to overcome the

School of Physics and Electronic Engineering, Yancheng Teachers University, Yancheng, 224051, PR China. E-mail: zhuanggc@yctu.edu.cn; chenxbok@126.com

† Electronic supplementary information (ESI) available. See DOI: 10.1039/d0ra10067f



process restrictions previously mentioned, especially high temperature and low pressure. Here, we present a new process to efficiently synthesize G supported $\text{Pt}_x\text{Fe}_{1-x}$ alloy nanoparticles using a atmospheric plasma reaction technology at near room temperature under atmospheric pressure.

For the chemical stability and the rapid injection rate of electrons from excited dye into TiO_2 conduction band, TiO_2 is normally used for photoanode material of DSSCs to load dye and transport electrons.^{22,23} But the non-favorable high recombination reaction rates of photo-induced electrons and holes between the interface of TiO_2 and electrolyte hinder the improvement of the power conversion efficiency (PCE) of the DSSCs performance.^{24–26} Thus, TiO_2 matrix in combination with a thin conducting layer (such as G) which can reduce the recombination of photo-induced charge carrier and accelerate the electron transport is utilized as effective photoanode. The incorporation of G in TiO_2 -based composite photoanodes to enhance the efficiency of the DSSCs has been an active issue among researchers over the last decade.^{27–32} Although many groups have already used the PtM alloys/G CEs and TiO_2 -based composite photoanodes separately to enhance the efficiency of DSSCs, in this work, we used both PtM alloys/G CE and TiO_2 /G photoanode simultaneously to improve the efficiency of devices.

Herein, $\text{Pt}_x\text{Fe}_{1-x}$ alloy/G nanohybrid CE material and TiO_2 /G photoanode material were prepared by a facile atmospheric plasma reaction route. It is expected that $\text{Pt}_x\text{Fe}_{1-x}$ alloy/G nanohybrids with a small amount of Pt will combine both high conductivity and high catalytic activity to reduce triiodide to iodide ions at the CE. As the results, the highest electrical conductivity and electrocatalytic ability were obtained for $\text{Pt}_{0.7}\text{Fe}_{0.3}$ /G electrode. Thus, a PCE of 10.13% was obtained for the DSSC device with $\text{Pt}_{0.7}\text{Fe}_{0.3}$ /G CE and TiO_2 /G photoanode.

2. Experimental

2.1. Synthesis of the PtFe alloy/G

G nanosheets and active carbon (AC) are purchased from Tanfeng Tech. Inc. (Suzhou, China). Other reagents are purchased from Sigma-Aldrich Shanghai Trading Co Ltd. and used without further purification. Pt/G, Fe/G, and PtFe alloy/G composites were synthesized by an atmospheric plasma reaction method using an AC plasma system. Fig. 1a shows a schematic diagram of the plasma system. Seven $\text{Pt}_x\text{Fe}_{1-x}$ /G composites with different volume ratios of Fe to Pt precursors were prepared for comparison. Firstly, 30 mg G was mixed thoroughly with 20 mL ethanol and ultrasonicated for 1 h to obtain a G dispersion solution. Secondly, two solutions of 1 mM of $\text{H}_2\text{PtCl}_6 \cdot x\text{H}_2\text{O}$ and 1 mM of $\text{Fe}(\text{NO}_3)_3$ in deionized water were prepared first. Then, the solutions were mixed at different volume ratios of 1 : 0, 0.9 : 0.1, 0.7 : 0.3, 0.5 : 0.5, 0.3 : 0.7, 0.1 : 0.9, and 0 : 1, and the total volume of the mixture was 50 mL. Thirdly, 20 mL G dispersion solution and 3 mL hydrazine hydrate were added in the above solution and stirred for 10 min. The reaction mixture was then transferred into the reactor of the plasma system at 200 W for 1 h. On completion, the black solid product was centrifuged, washed twice with DI water, followed by ethanol washing, and dried at 80 °C in vacuum. We denoted the CEs by

$\text{Pt}_0\text{Fe}_1/\text{G}$, $\text{Pt}_{0.1}\text{Fe}_{0.9}/\text{G}$, $\text{Pt}_{0.3}\text{Fe}_{0.7}/\text{G}$, $\text{Pt}_{0.5}\text{Fe}_{0.5}/\text{G}$, $\text{Pt}_{0.7}\text{Fe}_{0.3}/\text{G}$, $\text{Pt}_{0.9}\text{Fe}_{0.1}/\text{G}$, and $\text{Pt}_1\text{Fe}_0/\text{G}$.

2.2. Synthesis of the TiO_2 nanoparticles/G composite

Firstly, 20 mL of deionized water (DW) and 40 mL isopropyl alcohol were mixed together using magnetic stirrer until a homogeneous solution formed. Then, 6.0 g of titanium sulfate ($\text{Ti}(\text{SO}_4)_2$) was added under strong stirring till a uniform solution achieved. Secondly, 20 mL of G dispersion solution was slowly added to the above mixture under stirring. The reaction mixture was then transferred into the reactor of the plasma system at 150 W for 1 h. Finally, as-prepared TiO_2 nanoparticles/G were centrifuged, rinsed and overnight dried at 90 °C. The characterization results (see Fig. S1 and S2 in ESI†) and the corresponding discussion of the TiO_2 nanoparticles/G composite are shown in ESI.†

2.3. Electrode preparation, fabrication of DSSCs, characterization and measurements

Electrode preparation, fabrication of DSSCs, characterization and measurements are detailed in ESI.†

3. Results and discussion

3.1. Characterization of the $\text{Pt}_x\text{Fe}_{1-x}$ alloy/G nanohybrid materials

The stoichiometric ratio of Pt and Fe in $\text{Pt}_x\text{Fe}_{1-x}$ alloy/G was controlled to obtain an efficient $\text{Pt}_x\text{Fe}_{1-x}$ alloy/G CE with both good catalytic activity and electrical conductivity. Fig. 1b–h shows the SEM images of $\text{Pt}_0\text{Fe}_1/\text{G}$, $\text{Pt}_{0.1}\text{Fe}_{0.9}/\text{G}$, $\text{Pt}_{0.3}\text{Fe}_{0.7}/\text{G}$, $\text{Pt}_{0.5}\text{Fe}_{0.5}/\text{G}$, $\text{Pt}_{0.7}\text{Fe}_{0.3}/\text{G}$, $\text{Pt}_{0.9}\text{Fe}_{0.1}/\text{G}$, and $\text{Pt}_1\text{Fe}_0/\text{G}$ samples, respectively. It can be seen that the $\text{Pt}_x\text{Fe}_{1-x}$ NPs are firmly wrapped on the 2D like G nanosheets with a high surface coverage and high loading of $\text{Pt}_x\text{Fe}_{1-x}$ NPs. G nanosheets associated with each other are clearly visible in these figures. Such 3D-network architecture of G nanosheets with large accessible surface area and high $\text{Pt}_x\text{Fe}_{1-x}$ particle coverage on the surface is favorable for electrochemical catalytic activity of $\text{Pt}_x\text{Fe}_{1-x}$ alloy/G electrode for DSSC, because it provides numerous channels for rapid diffusion of I_3^- ions across the $\text{Pt}_x\text{Fe}_{1-x}/\text{G}$ thin layer, and this is a major requirement for the high electrochemical catalytic activity in the $\text{Pt}_x\text{Fe}_{1-x}/\text{G}$ CEs.

The TEM and HRTEM measurements were conducted to provide in-depth information about the morphology and structure of the $\text{Pt}_x\text{Fe}_{1-x}/\text{G}$. It should be mentioned that G nanosheets were used as a support for $\text{Pt}_x\text{Fe}_{1-x}$ NPs to simplify sample preparation steps. Take $\text{Pt}_{0.7}\text{Fe}_{0.3}/\text{G}$ for instance, the Fig. 2a displays the morphology of as-synthesized $\text{Pt}_{0.7}\text{Fe}_{0.3}/\text{G}$, and it shows the $\text{Pt}_{0.7}\text{Fe}_{0.3}$ nanoparticles of size around 50 nm immobilized on the graphene surface. The clear lattice fringes (Fig. 2b) with atomic spacing value (0.22 nm) are equivalent to (1 1 1) plane of a chemically ordered face centered tetragonal PtFe phase.³³ To determine the position of atoms on $\text{Pt}_{0.7}\text{Fe}_{0.3}/\text{G}$ electrode, elemental mapping was carried out to investigate the distribution of different species (Fig. 2c–f). Elemental mapping images confirm the presence of different elements (C, Pt and Fe) and also reveal the uniform distribution of C, Pt and Fe at the electrode surface. Fig. S3† shows

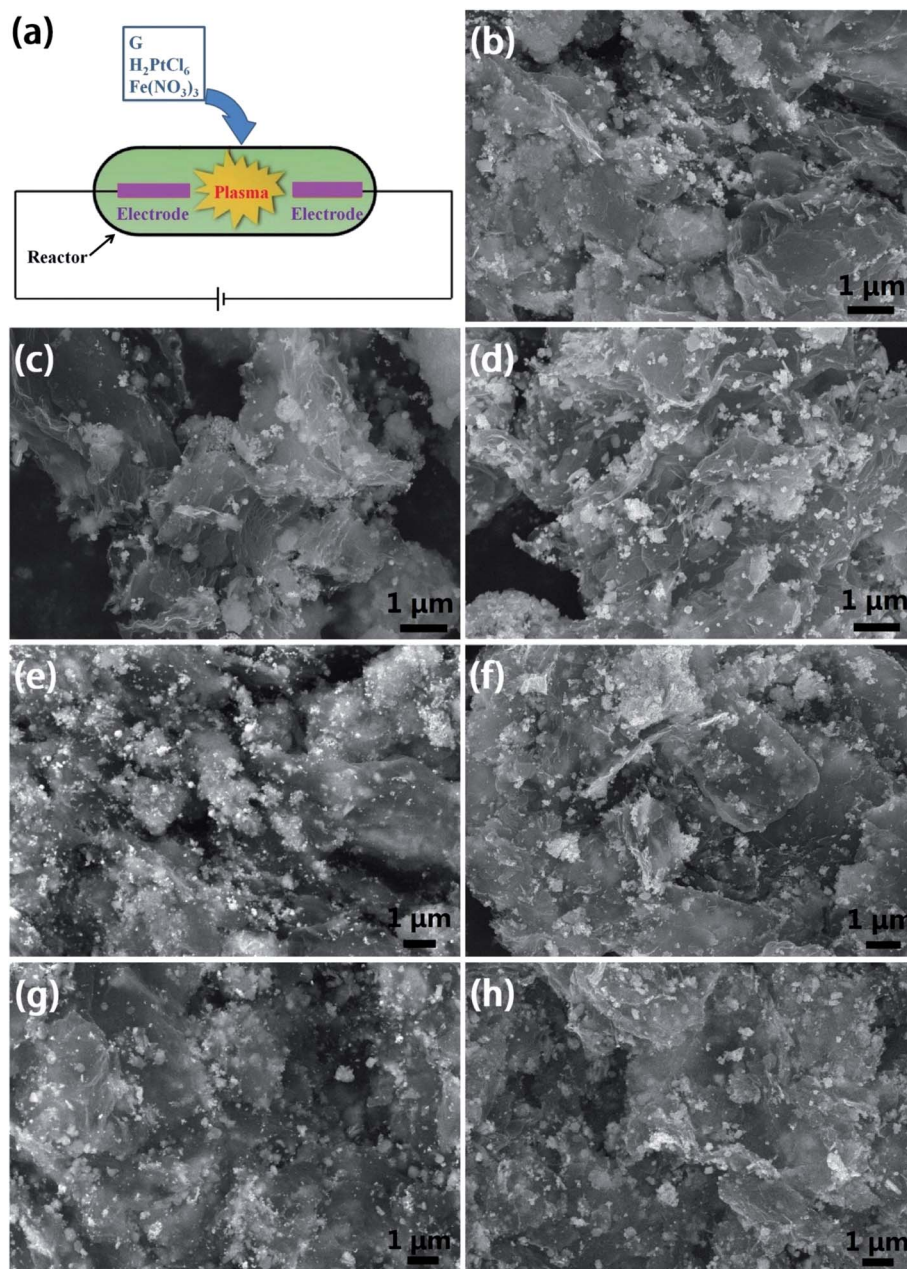


Fig. 1 (a) Schematic diagram of the plasma system. SEM images of CEs: (b) $\text{Pt}_0\text{Fe}_1/\text{G}$, (c) $\text{Pt}_{0.1}\text{Fe}_{0.9}/\text{G}$, (d) $\text{Pt}_{0.3}\text{Fe}_{0.7}/\text{G}$, (e) $\text{Pt}_{0.5}\text{Fe}_{0.5}/\text{G}$, (f) $\text{Pt}_{0.7}\text{Fe}_{0.3}/\text{G}$, (g) $\text{Pt}_{0.9}\text{Fe}_{0.1}/\text{G}$, and (h) $\text{Pt}_1\text{Fe}_0/\text{G}$.

the Raman spectrum of $\text{Pt}_{0.5}\text{Fe}_{0.5}/\text{G}$. It can be seen clearly that the peaks mainly originated from G. Raman spectrum of $\text{Pt}_{0.5}\text{Fe}_{0.5}/\text{G}$ displayed distinct G-band at 1580 cm^{-1} and D-band peak at 1350 cm^{-1} . The intensity ratio $I_{\text{D}}/I_{\text{G}}$ is about 1.12, illustrating a high defective structure of the used G.³⁴ We provided a study on the optimization of the chemical structure of the $\text{Pt}_x\text{Fe}_{1-x}/\text{G}$ composites in order to enhance both the electrical conductivity of CE and electrochemical catalytic activity for the reduction of I_3^- . Therefore, a set of CEs based on $\text{Pt}_x\text{Fe}_{1-x}/\text{G}$ composites prepared with different Pt precursor volume ratio was fabricated. It should be mentioned that the molar ratios of $[\text{Fe}]/[\text{Pt}]$ in the reaction precursors did not precisely match the Pt to Fe atomic ratios in corresponding to $\text{Pt}_x\text{Fe}_{1-x}$ alloy particles, as determined by the XPS analysis. The

chemical compositions of the $\text{Pt}_x\text{Fe}_{1-x}/\text{G}$ samples were evaluated to be $\text{Pt}_0\text{Fe}_1/\text{G}$, $\text{Pt}_{0.43}\text{Fe}_{0.57}/\text{G}$, $\text{Pt}_{0.56}\text{Fe}_{0.44}/\text{G}$, $\text{Pt}_{0.80}\text{Fe}_{0.20}/\text{G}$, $\text{Pt}_{0.82}\text{Fe}_{0.18}/\text{G}$, $\text{Pt}_{0.89}\text{Fe}_{0.11}/\text{G}$, and $\text{Pt}_1\text{Fe}_0/\text{G}$ (Table S1†).

The $\text{Pt}_x\text{Fe}_{1-x}/\text{G}$ nanohybrids are subjected to XPS measurement to determine the composition and electronic state of the elements, and the corresponding results are presented in Fig. S4 and Table S1.† As shown in Fig. S4b,† the binding energy for Fe $2p_{3/2}$ in $\text{Pt}_0\text{Fe}_1/\text{G}$ sample is centered at 708.1 eV, referring to metallic Fe. Take sample $\text{Pt}_{0.5}\text{Fe}_{0.5}/\text{G}$ for instance, the Fe $2p_{3/2}$ showed significantly positive shift of binding energy to 716.2 eV, which is probably due to the strengthened Fe–Pt bonding, *i.e.*, the alloying of Pt and Fe. The binding energy of Pt 4f locates at 71.3 eV and 74.6 eV, approving the metallic nature of Pt in



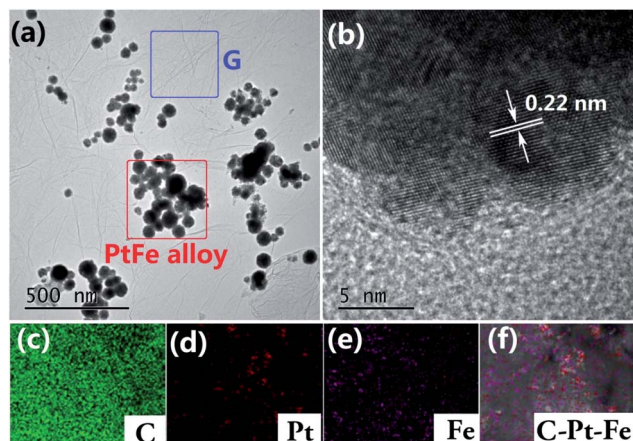


Fig. 2 (a and b) TEM images showing the $\text{Pt}_{0.7}\text{Fe}_{0.3}/\text{G}$; elemental mapping of $\text{Pt}_{0.7}\text{Fe}_{0.3}/\text{G}$: (c) C, (d) Fe, (e) Pt and (f) C–Pt–Fe.

$\text{Pt}_x\text{Fe}_{1-x}/\text{G}$ nanohybrid CEs.³⁵ The metallic bonds between Fe and Pt can result in a charge transfer from Fe to Pt and electronic redistribution on Pt surface, leading to a shift of the position of the Fe $2p_{3/2}$ peak to a higher binding energy.³⁶ According to the results from TEM photograph, elemental mapping and XPS spectra, it might be concluded that the obtained $\text{Pt}_x\text{Fe}_{1-x}/\text{G}$ CE catalysts are composed of metallic Pt, metallic Fe and PtFe alloy. The DSSCs performance is firmly associated with the generation, transfer, trapping, and transfer recombination of charge carrier. In general, a strong intensity of PL spectra indicates serious charge carrier recombination.³⁷ And, low trap density, high carrier mobility and efficient charge transfer process are the key parameters to reduce the photogenerated charge carrier recombination.³⁸ The photoluminescence (PL) spectra of the $\text{Pt}_x\text{Fe}_{1-x}/\text{G}$ nanocomposites are shown in Fig. S5.† One can observe lower PL peak intensities for PtFe alloy/G samples compared to pure Pt or Fe/G samples. Importantly, the $\text{Pt}_{0.7}\text{Fe}_{0.3}/\text{G}$ sample exhibits the lowest fluorescence intensity. This is positive enhance the photovoltaic performance.

3.2. Cyclic voltammetry measurements

The electrocatalytic properties of the CEs with respect to I_3^-/I^- ions in I^-/I_3^- redox couple was evaluated by cyclic voltammograms (CV), electrochemical impedance spectroscopy (EIS) and

Tafel polarization studies. Fig. 3 shows the CV curves of the prepared $\text{Pt}_0\text{Fe}_1/\text{G}$, $\text{Pt}_{0.1}\text{Fe}_{0.9}/\text{G}$, $\text{Pt}_{0.3}\text{Fe}_{0.7}/\text{G}$, $\text{Pt}_{0.5}\text{Fe}_{0.5}/\text{G}$, $\text{Pt}_{0.7}\text{Fe}_{0.3}/\text{G}$, $\text{Pt}_{0.9}\text{Fe}_{0.1}/\text{G}$, and $\text{Pt}_1\text{Fe}_0/\text{G}$ CEs. To probe the electrocatalytic activities of various CEs, the reduction current (J_{red}) and peak-to-peak separation (ΔE) of each CV plot were estimated. The $|J_{\text{red}}|$ and ΔE values are listed in Table 1. We can see that $|J_{\text{red}}|$ increases when the volume ratio of the Pt to Fe precursor decreases from 0 : 1 to 0.7 : 0.3 and that it decreases when the volume ratio of Pt to Fe decreases from 0.7 : 0.3 to 1 : 0. The $\text{Pt}_{0.7}\text{Fe}_{0.3}/\text{G}$ CE exhibits the highest $|J_{\text{red}}|$ value, indicating a higher charge transfer (redox reaction) rate across the $|J_{\text{red}}|$ CE compared to those of other electrodes. These results reveal that the highest $|J_{\text{red}}|$ value was achieved for $\text{Pt}_{0.7}\text{Fe}_{0.3}/\text{G}$ CE. The stability of the $\text{Pt}_{0.7}\text{Fe}_{0.3}/\text{G}$ electrode was further revealed by continuous CV measurements over 100 cycles (Fig. 3b). A slight change in curve shape and no change in J_{red} and J_{oxd} values can be observed in $\text{Pt}_{0.7}\text{Fe}_{0.3}/\text{G}$ CE even after 100 cycles of scan, and this suggests that the CEs are very stable in I_3^-/I^- electrolyte. The obtained results indicate the good electrochemical stability of $\text{Pt}_{0.7}\text{Fe}_{0.3}/\text{G}$ CE in I^-/I_3^- electrolyte. As presented in Table 1, ΔE is followed the sequence of $\text{Pt}_0\text{Fe}_1/\text{G}$ (430 mV) > $\text{Pt}_{0.1}\text{Fe}_{0.9}/\text{G}$ (417 mV) > $\text{Pt}_{0.3}\text{Fe}_{0.7}/\text{G}$ (416 mV) > $\text{Pt}_{0.5}\text{Fe}_{0.5}/\text{G}$ (412 mV) > $\text{Pt}_{0.7}\text{Fe}_{0.3}/\text{G}$ (373 mV) > $\text{Pt}_{0.9}\text{Fe}_{0.1}/\text{G}$ (389 mV) > $\text{Pt}_1\text{Fe}_0/\text{G}$ (402 mV). ΔE of 373 mV for $\text{Pt}_{0.7}\text{Fe}_{0.3}/\text{G}$ was the lowest value among all CEs which indicates the highest rate of the redox reaction of I_3^-/I^- .^{39,40}

3.3. Electrochemical impedance spectroscopy measurements

We conducted the EIS analysis to investigate the interfacial charge transfer process of the CEs and the influence of the electrochemical characteristics on the device performance. Nyquist plots obtained from various symmetrical dummy cell fabricated with sandwich-like structure (CE/electrolyte/CE) are presented in Fig. 4. The equivalent circuit is shown in the inset of Fig. 4a, and it is obtained by fitting the Nyquist plots with Z-View software, and the fit parameters (R_h , R_{trns} and R_{ct} values) are summarized in Table 1. Both ohmic internal resistance (R_h) and charge transfer resistance (R_{ct}) decrease with increasing the volume ratio of the Pt to Fe precursor from 0 : 1 to 0.7 : 0.3. However, further increase of the volume percentage of Pt

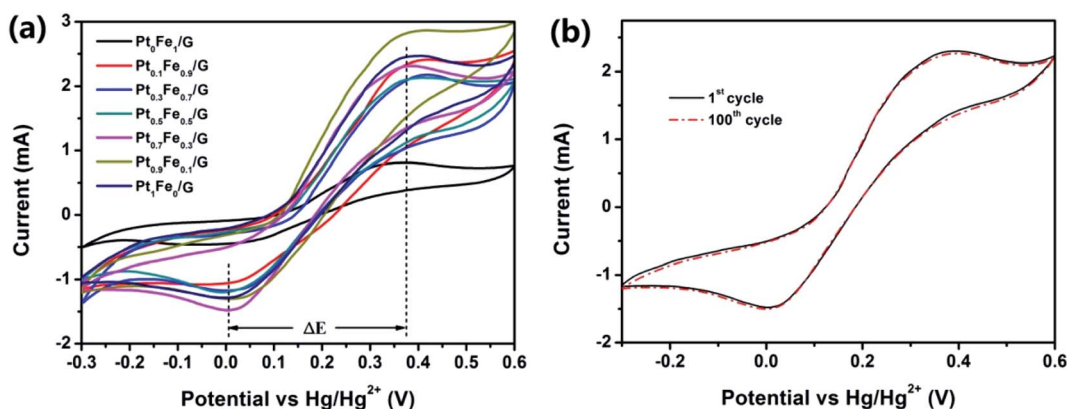


Fig. 3 (a) CV plots of electrodes and (b) CV curves of the $\text{Pt}_{0.7}\text{Fe}_{0.3}/\text{G}$ measured with 100 cycles.



Table 1 Properties of $\text{Pt}_x\text{Fe}_{1-x}/\text{G}$ CEs extracted from the CV, EIS and Tafel measurements^a

| Counter electrode | $ J_{\text{red}} $ (mA) | ΔE (mV) | R_h (Ω) | R_{trns} (Ω) | R_{ct} (Ω) | J_0 (mA) | J_0^b (mA) | J_{lim} (mA) |
|---|-------------------------|-----------------|--------------------|--------------------------------|------------------------------|------------|--------------|-----------------------|
| $\text{Pt}_0\text{Fe}_1/\text{G}$ | 0.460 | 430 | 5.84 | 0.58 | 15.6 | 2.05 | 1.20 | 12.11 |
| $\text{Pt}_{0.1}\text{Fe}_{0.9}/\text{G}$ | 1.077 | 417 | 5.69 | 0.27 | 8.22 | 3.90 | 2.40 | 14.06 |
| $\text{Pt}_{0.3}\text{Fe}_{0.7}/\text{G}$ | 1.169 | 416 | 5.62 | 0.24 | 4.67 | 6.87 | 2.98 | 17.02 |
| $\text{Pt}_{0.5}\text{Fe}_{0.5}/\text{G}$ | 1.201 | 412 | 5.57 | 0.17 | 4.02 | 7.98 | 4.73 | 19.41 |
| $\text{Pt}_{0.7}\text{Fe}_{0.3}/\text{G}$ | 1.479 | 373 | 5.48 | 0.12 | 2.86 | 11.22 | 7.46 | 25.58 |
| $\text{Pt}_{0.9}\text{Fe}_{0.1}/\text{G}$ | 1.301 | 389 | 5.73 | 0.61 | 4.13 | 7.77 | 5.71 | 23.33 |
| $\text{Pt}_1\text{Fe}_0/\text{G}$ | 1.283 | 402 | 5.82 | 0.83 | 3.95 | 8.12 | 5.14 | 21.73 |

^a J_{red} : peak current density of the reduction, ΔE : peak-to-peak separation. ^b The data were calculated from the Tafel curves in Fig. 5.

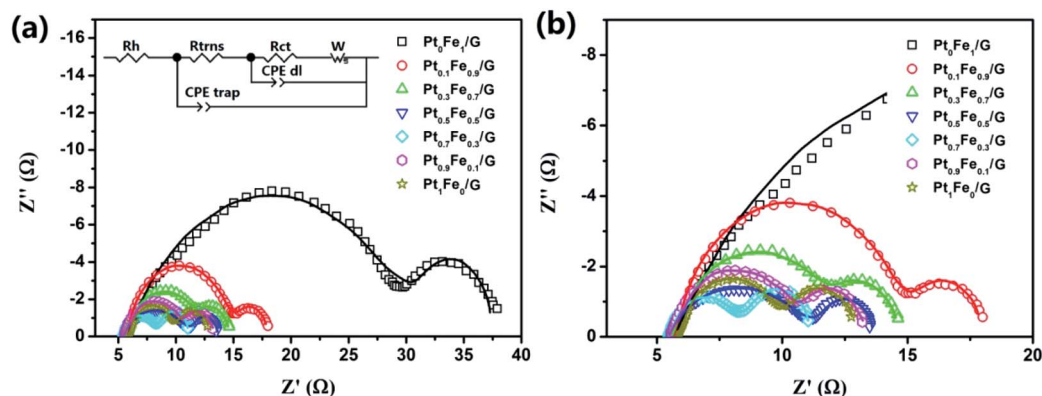


Fig. 4 (a and b) Nyquist plots of the symmetrical cells fabricated with two identical CEs. The inset shows the equivalent circuit model for fitting.

precursor led to increase in the R_{ct} value. The R_{ct} value of the $\text{Pt}_{0.7}\text{Fe}_{0.3}/\text{G}$ CE (2.86 Ω) was the smallest among those recorded for other CEs. The relationship between the exchange current density (J_0) and R_{ct} is $J_0 = RT/nFR_{\text{ct}}$, where R is the gas constant, T is the temperature, n is the number of electrons involved in the reduction of the iodide electrolyte, and F is Faraday's constant. The resulting J_0 values are shown in Table 1. It is worth noting that a high J_0 value indicates a high fill factor (FF) and a high short-circuit current density (J_{sc}) in the DSSC.⁴¹

Considering that the parameter R_{trns} is inversely proportional to electrode conductivity,⁴² we can conclude that the conductivity of $\text{Pt}_1\text{Fe}_0/\text{G}$ CE is significantly lower compared with that of other $\text{Pt}_x\text{Fe}_{1-x}/\text{G}$. This phenomenon can be attributed to the synergistic effect of G with the deposited PtFe alloy nanoparticles as well as the synergistic effect of degree of alloying Fe with Pt. The results also indicate that the synergistic effect of G nanosheets with Pt_0Fe_1 nanoparticles was higher than that of G nanosheets with Pt_1Fe_0 . That is to say, the PtFe alloy/G facilitates electron transfer. In addition, it is shown that R_{trns} value of $\text{Pt}_{0.7}\text{Fe}_{0.3}/\text{G}$ was the smallest among all $\text{Pt}_x\text{Fe}_{1-x}/\text{G}$ CEs (Table 1), indicating the highest electrical conductivity of $\text{Pt}_{0.7}\text{Fe}_{0.3}/\text{G}$ CE.

3.4. Tafel measurements

In order to further investigate the synergistic effect and electrocatalytic activity, Tafel measurements were performed. From the corresponding Tafel zone and diffusion zone, we can get the exchange current density (J_0) and the limiting diffusion current density (J_{lim}), respectively. The results are presented in Fig. 5

and Table 1. In theory, J_0 is directly related to the electrocatalytic ability of the CE and can be generated from the intersection of the cathodic branch and the equilibrium potential line.⁴³ It was found that the trend of the variation in the J_0 values are in the order of $\text{Pt}_{0.7}\text{Fe}_{0.3}/\text{G} > \text{Pt}_{0.9}\text{Fe}_{0.1}/\text{G} > \text{Pt}_1\text{Fe}_0/\text{G} > \text{Pt}_{0.5}\text{Fe}_{0.5}/\text{G} > \text{Pt}_{0.3}\text{Fe}_{0.7}/\text{G} > \text{Pt}_{0.1}\text{Fe}_{0.9}/\text{G} > \text{Pt}_0\text{Fe}_1/\text{G}$, indicating that the electrocatalytic ability of $\text{Pt}_{0.7}\text{Fe}_{0.3}/\text{G}$ CE is better than that of other five CEs. Clearly, the J_0 values deduced from Tafel plots follow the same trend, as we observed in EIS analysis. The intersection of the cathodic branch with the Y-axis can be considered as the J_{lim} . It should be noted that J_{lim} has a positive relationship with diffusion coefficient (D) and can be expressed as $D = lJ_{\text{lim}}/2nFC$,

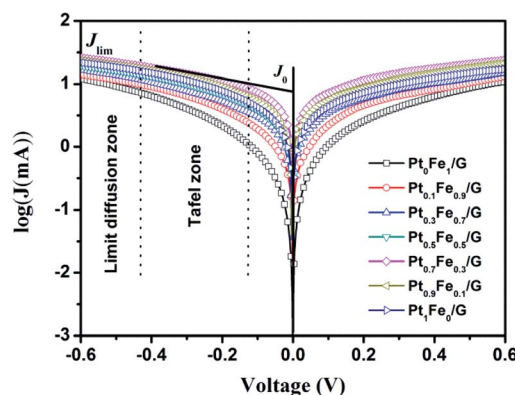


Fig. 5 Tafel polarization of different dummy cells that are same as those used for the EIS measurements.



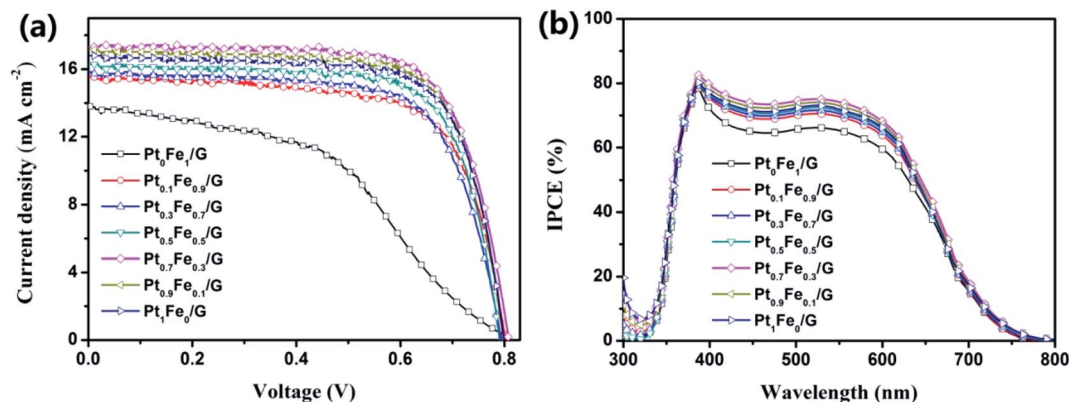


Fig. 6 (a) Current density–voltage curves of DSSCs with different CEs. (b) IPCE curves of different devices.

where l and C denote the spacer thickness and electrolyte concentration, respectively. Thus, a larger J_{lim} value indicates a higher diffusion rate for the I^-/I_3^- redox couple in the electrolyte.⁴⁴ The highest J_{lim} value was found for the $\text{Pt}_{0.7}\text{Fe}_{0.3}/\text{G}$ electrode, which indicates a higher diffusion coefficient for the redox couple in the electrolyte. Both EIS and Tafel studies support the relatively high efficiency of the $\text{Pt}_{0.7}\text{Fe}_{0.3}/\text{G}$ CE based DSSC, as it is demonstrated below.

According to the above electrochemical analysis, it was found that the electrocatalytic activity and charge-transfer ability of these $\text{Pt}_x\text{Fe}_{1-x}/\text{G}$ CEs have been markedly enhanced in comparison with pristine Pt/G CE. This finding can be explained by the alloying effect of transition metals with Pt.^{45,46} Furthermore, electrocatalytic activity dependence on Pt/Fe stoichiometric ratio of the $\text{Pt}_x\text{Fe}_{1-x}/\text{G}$ CEs was observed. This can be attributed to the electronic structure changes upon alloying Pt with Fe.¹¹

3.5. Photovoltaic performance

We discuss the effect of CEs on the photovoltaic (PV) performance of DSSCs. The photocurrent–voltage (J – V) characteristics are shown in Fig. 6a and S6,[†] and the PV parameters are presented in Table 2. We found that the device efficiencies follow the sequence of $\text{Pt}_{0.7}\text{Fe}_{0.3}/\text{G}$ (10.13%) > $\text{Pt}_{0.9}\text{Fe}_{0.1}/\text{G}$ (9.89%) > $\text{Pt}_1\text{Fe}_0/\text{G}$ (9.72%) > $\text{Pt}_{0.5}\text{Fe}_{0.5}/\text{G}$ (9.30%) > $\text{Pt}_{0.3}\text{Fe}_{0.7}/\text{G}$ (8.75%) > $\text{Pt}_{0.1}\text{Fe}_{0.9}/\text{G}$ (8.62%) > $\text{Pt}_0\text{Fe}_1/\text{G}$ (5.08%). Note that the DSSC with $\text{Pt}_{0.7}\text{Fe}_{0.3}/\text{G}$ CE yields a remarkable power conversion efficiency

of 10.13% ($J_{\text{sc}} = 17.29 \text{ mA cm}^{-2}$, $V_{\text{oc}} = 808 \text{ mV}$, and $\text{FF} = 72.45\%$) in comparison to 9.72% for $\text{Pt}_1\text{Fe}_0/\text{G}$ CE based DSSC. As noted previously, the difference in the V_{oc} values was supported by ΔE .⁴⁰ It is shown that the FF values ranged from 46.02 to 72.45%, and the trend of the FF value was similar to those of the catalytic activity revealed in the electrochemical measurements (CV, EIS, and Tafel). The low series resistance of a DSSC, which mainly depends on the R_{ct} at the CE/electrolyte interface (evidenced by EIS analysis), can be used to explain this result.⁴⁷ We see in Table 2 that the J_{sc} value of the DSSC based on $\text{Pt}_{0.7}\text{Fe}_{0.3}/\text{G}$ CE was found to be the highest value among the DSSCs fabricated from $\text{Pt}_x\text{Fe}_{1-x}/\text{G}$ CEs. The incident photocurrent efficiency (IPCE) performance tests were conducted with same electrolyte solution to further confirm the change in J_{sc} values. The resultant IPCE spectra are presented in Fig. 6b. The IPCE of the $\text{Pt}_{0.7}\text{Fe}_{0.3}$ CE based DSSC was higher than that of the other $\text{Pt}_x\text{Fe}_{1-x}/\text{G}$ CE based device over the visible wavelength. Higher the IPCE, greater will be the J_{sc} value. It was found that the change in the J_{sc} values is followed the sequence of $\text{Pt}_{0.7}\text{Fe}_{0.3}/\text{G}$ (17.99 mA cm^{-2}) > $\text{Pt}_{0.9}\text{Fe}_{0.1}/\text{G}$ (17.65 mA cm^{-2}) > $\text{Pt}_1\text{Fe}_0/\text{G}$ (17.12 mA cm^{-2}) > $\text{Pt}_{0.5}\text{Fe}_{0.5}/\text{G}$ (17.05 mA cm^{-2}) > $\text{Pt}_{0.3}\text{Fe}_{0.7}/\text{G}$ (16.14 mA cm^{-2}) > $\text{Pt}_{0.1}\text{Fe}_{0.9}/\text{G}$ (15.61 mA cm^{-2}) > $\text{Pt}_0\text{Fe}_1/\text{G}$ (13.67 mA cm^{-2}). The obtained results are in good accordance with the change of J_{sc} in the PV performances. The highest J_{sc} value of 17.99 mA cm^{-2} was found in the cell with the $\text{Pt}_{0.7}\text{Fe}_{0.3}/\text{G}$ electrode which is due to the high electrochemical catalytic activity of the CEs. The higher catalytic activity leads to

Table 2 Photovoltaic properties of DSSCs with $\text{Pt}_x\text{Fe}_{1-x}/\text{G}$ CEs

| Counter electrode | J_{sc} (mA cm^{-2}) | J_{sc}^a (mA cm^{-2}) | V_{oc} (mV) | FF (%) | η (%) |
|---|---|---|----------------------|--------|------------------|
| $\text{Pt}_0\text{Fe}_1/\text{G}$ | 13.79 | 13.67 | 799 | 46.02 | 5.08 ± 0.20 |
| $\text{Pt}_{0.1}\text{Fe}_{0.9}/\text{G}$ | 15.52 | 15.61 | 802 | 69.25 | 8.62 ± 0.15 |
| $\text{Pt}_{0.3}\text{Fe}_{0.7}/\text{G}$ | 15.83 | 16.14 | 794 | 69.63 | 8.75 ± 0.13 |
| $\text{Pt}_{0.5}\text{Fe}_{0.5}/\text{G}$ | 16.28 | 17.05 | 790 | 72.26 | 9.30 ± 0.19 |
| $\text{Pt}_{0.7}\text{Fe}_{0.3}/\text{G}$ | 17.29 | 17.99 | 808 | 72.45 | 10.13 ± 0.11 |
| $\text{Pt}_{0.9}\text{Fe}_{0.1}/\text{G}$ | 17.13 | 17.65 | 797 | 72.44 | 9.89 ± 0.12 |
| $\text{Pt}_1\text{Fe}_0/\text{G}$ | 16.77 | 17.12 | 799 | 72.42 | 9.72 ± 0.17 |

^a The values are obtained from IPCE measurements.



an increase in the reduction rate of I_3^- to I^- , which subsequently diffuse into the working electrode for the ground state recovery of the dye N719. As shown in Fig. S7,† the long-term stability of DSSCs with different Pt_xFe_{1-x}/G CEs for 20 days was presented. There are only slight decreases in efficiency values, and it indicates that Pt_xFe_{1-x}/G CE materials can be used as good CE alternatives to traditional Pt electrode for DSSCs. It was revealed that 86.4% of the PEC value is kept for Pt_0Fe_1/G CE based DSSC in comparison to 92.6%, 95.8%, 96.0%, 95.4%, 94.8% and 89.1% for the devices with $Pt_{0.1}Fe_{0.9}/G$, $Pt_{0.3}Fe_{0.7}/G$, $Pt_{0.5}Fe_{0.5}/G$, $Pt_{0.7}Fe_{0.3}/G$, $Pt_{0.9}Fe_{0.1}/G$, and Pt_1Fe_0/G , respectively. Obviously, pure Pt or pure Fe/G CE based DSSC exhibited relatively weak lower long-term stability. This result can be explained by the research findings of Tang and coworkers.⁴⁸ In their report, the authors have carefully described the chemical dissolution of alloy CE in a real liquid-junction DSSC device. They pointed out that the competitive reactions of Fe element with I_3^-/I^- can restrict the dissolution of Pt species and therefore protect the high catalytic activity of CEs.

4. Conclusion

In this study, well-dispersed Pt_xFe_{1-x} nanoparticles were anchored on G by a facile one-step atmospheric plasma reaction method. By controlling the volume ratio of Pt and Fe precursors, the chemical composition of the Pt_xFe_{1-x}/G can be easily tuned, as confirmed in an XPS analysis. The optimization of the chemical composition of the Pt_xFe_{1-x}/G nanohybrid resulted in optimizing the catalytic activity toward a reduction of triiodide ions, as reflected by the smallest series resistance values and charge transfer resistance values at the electrolyte/counter electrode interface. In addition, TiO_2 nanoparticles/G photoanode material was prepared by atmospheric plasma reaction method. As a result, the DSSCs using $Pt_{0.7}Fe_{0.3}/G$ CE and TiO_2 nanoparticles/G photoanode obtained PCE of 10.13% which is higher than Pt_1Fe_0/G CE (9.72%). The excellent electrocatalytic properties, simple synthesis process, and the low-cost of the $Pt_{0.7}Fe_{0.3}/G$ CE suggest that the $Pt_{0.7}Fe_{0.3}/G$ CE is very promising as a cost-effective stable CEs for efficient and inexpensive DSSCs.

Conflicts of interest

There are no conflicts to declare.

Acknowledgements

This work was supported by the Qing Lan Project of Jiangsu Province.

References

- 1 B. O. Regan and M. Gratzel, *Nature*, 1991, **353**, 737–781.
- 2 N. G. Park, *J. Electrochem. Sci. Technol.*, 2010, **1**, 69–74.
- 3 Y. Hou, D. Wang, X. H. Yang, W. Q. Fang, B. Zhang, H. F. Wang, G. Z. Lu, P. Hu, H. J. Zhao and H. G. Yang, *Nat. Commun.*, 2013, **4**, 1–8.
- 4 N. Papageorgiou, *Coord. Chem. Rev.*, 2004, **248**, 1421–1446.
- 5 N. J. Song, C. M. Chen, C. Lu, Z. Liu, Q. Q. Kong and R. Cai, *J. Mater. Chem. A*, 2014, **2**, 16563–16568.
- 6 L. Zhang, H. K. Mulmudi, S. K. Batabyal, Y. M. Lam and S. G. Mhaisalkar, *Phys. Chem. Chem. Phys.*, 2012, **14**, 9906–9911.
- 7 K. P. Acharya, H. Khatri, S. Marsillac, B. Ullrich and M. Zamkov, *Appl. Phys. Lett.*, 2010, **97**, 201108.
- 8 J. Liu, Q. Tang and B. He, *J. Power Sources*, 2014, **268**, 56–62.
- 9 J. Liu, Q. Tang, B. He and L. Yu, *J. Power Sources*, 2015, **282**, 79–86.
- 10 Y. Zhou, R. Neyerlin, R. S. Olson, R. Pylypenko, R. Bult, R. N. Dinh, R. Gennett, R. Shao and R. O'Hayre, *Energy Environ. Sci.*, 2010, **3**, 1437–1446.
- 11 V. D. Dao, L. L. Larina, Q. C. Tran, V.-T. Bui, V. T. Nguyen, T. D. Pham, I. M. A. Mohamed, N. A. M. Barakat, B. T. Huy and H. S. Choi, *Carbon*, 2017, **116**, 294–302.
- 12 K. H. Bae, E. Park, V. D. Dao and H. S. Choi, *J. Alloys Compd.*, 2017, **702**, 449–457.
- 13 V.-D. Dao, *Mater. Today Energy*, 2020, **16**, 100384.
- 14 V. D. Dao, Q. C. Tran, S. H. Ko and H. S. Choi, *J. Mater. Chem.*, 2013, **1**, 4436.
- 15 T. Morishita, T. Ueno, G. Panomsuwan, J. Hieda, A. Yoshida, M. A. Bratescu and N. Saito, *Sci. Rep.*, 2016, **6**, 36880.
- 16 X. Hu, X. Shen, O. Takai and N. Saito, *J. Alloys Compd.*, 2013, **552**, 351–355.
- 17 S. Fuldner, R. Mild, H. I. Siegmund, J. A. Schroeder, M. Gruber and B. König, *Green Chem.*, 2010, **12**, 400–406.
- 18 M. Ghavre, O. Byrne, L. Altes, P. K. Surolia, M. Spulak, B. Quilty, K. R. Thampi and N. Gathergood, *Green Chem.*, 2014, **16**, 2252–2265.
- 19 A. Yella, H. W. Lee, H. N. Tsao, C. Y. Yi, A. K. Chandiran, M. K. Nazeeruddin, E. W.-G. Diao, C.-Y. Yeh, S. M. Zakeeruddin and M. Grätzel, *Science*, 2011, **334**, 629–634.
- 20 M. Gratzel, *Chem. Lett.*, 2005, **34**, 8–13.
- 21 C.-Y. Chen, M. Wang, J.-Y. Li, N. Pootrakulchote, L. Alibabaei, C.-H. Ngoc-Le, J.-D. Decoppet, J.-H. Tsai, C. Grätzel, C.-G. Wu, S. M. Zakeeruddin and M. Gratzel, *ACS Nano*, 2009, **3**, 3103–3109.
- 22 Z. M. Yuan and L. W. Yin, *Nanoscale*, 2014, **6**, 13135–13144.
- 23 K. Pomoni, M. V. Sofianou, T. Georgakopoulos, N. Boukos and C. Trapalis, *J. Alloys Compd.*, 2013, **548**, 194–200.
- 24 E. Y. Guo and L. W. Yin, *J. Mater. Chem. A*, 2015, **3**, 13390–13401.
- 25 E. Y. Guo, L. W. Yin and L. Y. Zhang, *CrystEngComm*, 2014, **16**, 3403–3413.
- 26 E. Palomares, J. N. Clifford, S. A. Haque, T. Lutz and J. R. Durrant, *Chem. Commun.*, 2002, **14**, 1464–1465.
- 27 Y. B. Tang, C. S. Lee, J. Xu, Z. T. Liu, Z. H. Chen, Z. He, Y.-L. Cao, G. Yuan, H. Song, L. Chen, L. Luo, H.-M. Cheng, W.-J. Zhang, I. Bello and S.-T. Lee, *ACS Nano*, 2010, **4**, 3482–3488.
- 28 S. W. Chong, C. W. Lai and S. B. A. Hamid, *Materials*, 2016, **9**, 1–13.
- 29 H. Ma, J. Tian, L. Cui, Y. Liu and Z. Shan, *J. Mater. Chem. A*, 2015, **3**, 8890–8895.



- 30 H. S. Ko, H. J. Han, G. Na, A. R. Lee, J. J. Yun and E. M. Han, *Mol. Cryst. Liq. Cryst.*, 2013, **579**, 83–88.
- 31 F. W. Low, C. W. Lai and S. B. A. Hamid, *J. Mater. Sci.: Mater. Electron.*, 2017, **28**, 3819–3836.
- 32 A. Merazga, J. Al-Zahrani, A. Al-Baradi, B. Omer, A. Badawi and S. Al-Omairy, *Mater. Sci. Eng., B*, 2020, **259**, 114581.
- 33 S. Sun, C. B. Murray, D. Weller, L. Folks and A. Moser, *Science*, 2000, **87**, 1989–1992.
- 34 C. Nan, L. Zhan, H. Liao, M. K. Song, Y. Li and E. J. Cairns, *J. Am. Chem. Soc.*, 2014, **136**, 4659–4663.
- 35 B. Canava, J. Vigneron, A. Etcheberry, J. F. Guillemoles and D. Lincot, *Appl. Surf. Sci.*, 2002, **202**, 8–14.
- 36 J. A. Rodriguez and D. W. Goodman, *Science*, 1992, **257**, 897–903.
- 37 P. Wang, L. Zong, Z. Guan, Q. Li and J. Yang, *Nanoscale Res. Lett.*, 2018, **13**, 33.
- 38 B. Yang, F. Zhang, J. Chen, S. Yang, X. Xia, T. Pullerits, W. Deng and K. Han, *Adv. Mater.*, 2017, **29**, 1703758.
- 39 H. Tributsch, *Coord. Chem. Rev.*, 2004, **248**, 1511–1530.
- 40 V. D. Dao, S. H. Kim, H. S. Choi, J. H. Kim, H. O. Park and J. K. Lee, *J. Phys. Chem. C*, 2011, **115**, 25529–25534.
- 41 I. Hod, V. González-Pedro, Z. Tachan, F. Fabregat-Santiago, I. Mora-Seró, J. Bisquert and A. Zaban, *J. Phys. Chem. Lett.*, 2011, **2**, 3032–3035.
- 42 W. Kwon, J. M. Kim and S. W. Rhee, *Electrochim. Acta*, 2012, **68**, 110–113.
- 43 W. Wang, X. Pan, W. Liu, B. Zhang, H. Chen, X. Fang, J. Yao and S. Dai, *Chem. Commun.*, 2014, **50**, 2618–2620.
- 44 S. Yun, M. Wu, Y. Wang, J. Shi, X. Lin, A. Hagfeldt and T. Ma, *ChemSusChem*, 2013, **6**, 411–416.
- 45 H. Y. Park, D. H. Lim, S. J. Yoo, H. J. Kim, D. Henkensmeier, J. Y. Kim, H. C. Ham and J. H. Jang, *Sci. Rep.*, 2017, **7**, 1–9.
- 46 J. Zhang, M. Ma, Q. Tang and L. Yu, *J. Power Sources*, 2016, **303**, 243–249.
- 47 L. Han, N. Koide, Y. Chiba, A. Islam, R. Komiya, N. Fuke, A. Fukui and R. Yamanaka, *Appl. Phys. Lett.*, 2005, **86**, 737.
- 48 Q. Tang, H. Zhang, Y. Meng, B. He and L. Yu, *Angew. Chem., Int. Ed.*, 2015, **54**, 11448–11452.

